Direct Control of Electron Spin at Chiral Active Sites for Highly Efficient Oxygen Reduction Reaction

Xia Wang[1,7], Mayra Peralta[1,7], Xiaodong Li[2,7], Paul V. Möllers[3], Dong Zhou[4], Patrick Merz[1], Ulrich Burkhardt[1], Horst Borrmann[1], Robredo Magro Iñigo[1,6], Shekhar Chandra[1], Helmut Zacharias[3], Xinliang Feng[2,5*], Claudia Felser[1*]*

[1] Max-Planck-Institute for Chemical Physics of Solids, 01187, Dresden, Germany

[2] Centre for Advancing Electronics Dresden (cfaed) & Faculty of Chemistry and Food Chemistry, Technische Universität Dresden, 01062, Dresden, Germany

[3] Center for Soft Nanoscience, University of Münster, 48149, Münster, Germany

[4] Tsinghua Shenzhen International Graduate School, Tsinghua University, Shenzhen, 518055, China

[5] Max Planck Institute of Microstructure Physics, 06120, Halle, Germany

[6] Donostia International Physics Center, 20018, Donostia-San Sebastian, Spain

[7] These authors contributed equally to this work.

[*]Corresponding author.

E-mail: xia.wang@cpfs.mpg.de (X. Wang)

xinliang.feng@tu-dresden.de (X. Feng)

Claudia.Felser@cpfs.mpg.de (C. Felser)

Abstract

The oxygen reduction reaction (ORR) in acidic suffers from sluggish kinetics owing to the spin-dependent electron transfer process. However, the direct generation of spin-polarized electron at catalytic active sites remains elusive and the underlying mechanism is still controversial due to the lack of intrinsically homochiral catalysts. To address this challenge, we demonstrate the topological homochiral PdGa (TH PdGa) crystal with chiral active sites for ORR. Spin-resolved photoemission and theoretical simulations probed the in-situ generated spin polarizations at Pd sites. Both structural chirality and spin-orbital coupling are essential for inducing spin polarization. TH PdGa with remarkable concentration of spin-polarized electron outperforms the benchmark Pt/C by about 70 times in terms of kinetic current density at 0.85 V *vs.* the reversible hydrogen electrode (RHE) and over 200 times in terms of the turnover frequency. This work allows us to elucidate the respective contributions of spin polarization to the enhanced acidic ORR activity.

Introduction

The electrocatalytic oxygen reduction reaction (ORR) plays a critical role in determining the efficiency of sustainable energy conversion systems, such as metal-air batteries and fuel cells[1, 2]. However, the sluggish kinetics of the ORR, especially in acidic media, caused by the multi-electron transfer process, significantly restricts the performance of these devices.[3, 4, 5] The ORR involves a four-electron transfer process that starts from oxygen molecules with triplet states ($^3\Sigma_g^-$) while generating oxygen species/reaction products in singlet ground states ($^1\Delta$). Due to the non-conservation of electron spin during the conversion of triplet oxygen molecules, additional energy is required for this step, as it is forbidden by quantum mechanics.[6] Therefore, the control and understanding of the spin-dependent electron transfer process is essential for ORR in solid materials, which, however, has been neglected until now.

The chiral-induced spin selectivity (CISS) effect opens up a new way to manipulate the electron spin for chemical reactions such as oxygen electrocatalysis.[7, 8, 9, 10] In particular, CISS influences the electron spin transferred through chiral structures, thereby influencing the reaction kinetics and pathways for the ORR.[11, 12] As a result, it provides a promising possibility to improve the ORR activity and even go beyond the limitations of the volcano plot.[6, 13, 14] Nevertheless, previously reported chiral oxygen electrocatalysts are obtained by imparting chirality to initially achiral metal surfaces through adsorption of chiral molecules or imprinted chiral cavities.[12, 15, 16] The chiral molecules on the catalytic surface will sacrifice the accessibility of the active sites and reduce the overall conductivity as the chiral molecules are typically insulators. It remains unclear how the polarized electrons are transferred from the chiral molecules to the catalytic active sites and reaction species.[17] Furthermore, these "artificial chiral catalytic surfaces" make it difficult to understand the underlying mechanisms of the spin-dependent electron transfer process in chiral solids. Therefore, the pursuit of intrinsically chiral electrocatalysts with well-defined homochiral structures is prominent to understand the CISS effect in solids for ORR, and thus reveal the interplay between catalytic activity and chiral quantum properties such as spin-orbital coupling (SOC) and exotic spin/orbital angular momentum (SAM/OAM).[18, 19]

Topological homochiral PdGa (TH PdGa) crystal with space group $P2_13$ (No. 198) represents a unique material with intrinsically chiral geometrical and electronic structures.[20, 21] The electron spin at the crystal surface exhibits a spin-orbital momentum locking state due to the substantial spin-orbital coupling (SOC).[22] The chiral electronic structure of TH PdGa is characterized by chiral fermions and Fermi-arc surface states with reversed velocities.[23] Moreover, TH PdGa exhibits robust topological surface states (TSS) that are resistant to extrinsic modifications (doping, strain and defect, etc.), making it an ideal platform to study spin-dependent electron transfer processes at the catalytic surface.[24, 25, 26] Herein, we reveal the essential role of spin polarization on the enhancement of ORR kinetics and efficiency with TH PdGa as electrocatalyst. The spin polarization in the TH PdGa is directly probed through spin-resolved photoemission experiments, which reveals opposite spin polarization values for the two TH PdGa enantiomers. Compared to catalysts with "artificial chiral catalytic surfaces", the spin polarization concentration in TH-PdGa is about 10^7 orders of magnitude higher. Theoretical modelling further demonstrates the essential role of both the chiral structure and SOC for the generation of spin polarization at the catalytic active sites. As a result, TH PdGa exhibits exceptional ORR performance, such as a record high half-wave potential ($E_{1/2}$) of 0.89 V *vs.* RHE, a large kinetic current density of 137.02 mA cm^{-2} at 0.85 V *vs.* RHE and a turnover frequency of 16.1 s^{-1}, surpassing Pt/C with $E_{1/2}$ of 0.80 V *vs.* RHE, a kinetic current density of 1.97 mA cm^{-2} and a turnover frequency of 0.071 s^{-1}, respectively. In addition, TH PdGa shows the highest ORR selectivity with the lowest H_2O_2 production compared to Pt/C and achiral PdGa (AC PdGa), which is attributed to the spin polarization in TH PdGa. Our work represents a breakthrough in the development of high-performance intrinsic chiral catalysts for an acidic ORR by directly controlling the electron spin at the active sites, and opens up new possibilities for next-generation energy conversion technologies.

Results and discussion

Chiral crystal structure characterization of TH PdGa

The TH PdGa crystal in this study belongs to the B20 cubic space group (No.198) with a lattice constant of a = 4.897 Å. The bulk chiral structure of TH PdGa is distinguished by the helical arrangement of Pd or Ga atoms along the [111] direction, wherein PdGa

enantiomers exhibit either a clockwise or anticlockwise helix (Fig. 1a). Additionally, the topmost surface layers of Pd or Ga trimers exhibit opposite handedness on the threefold symmetric (111) crystal plane, enabling the surface chirality, and thus influencing the surface properties of the outermost Pd sites (Supplementary Fig. 1).

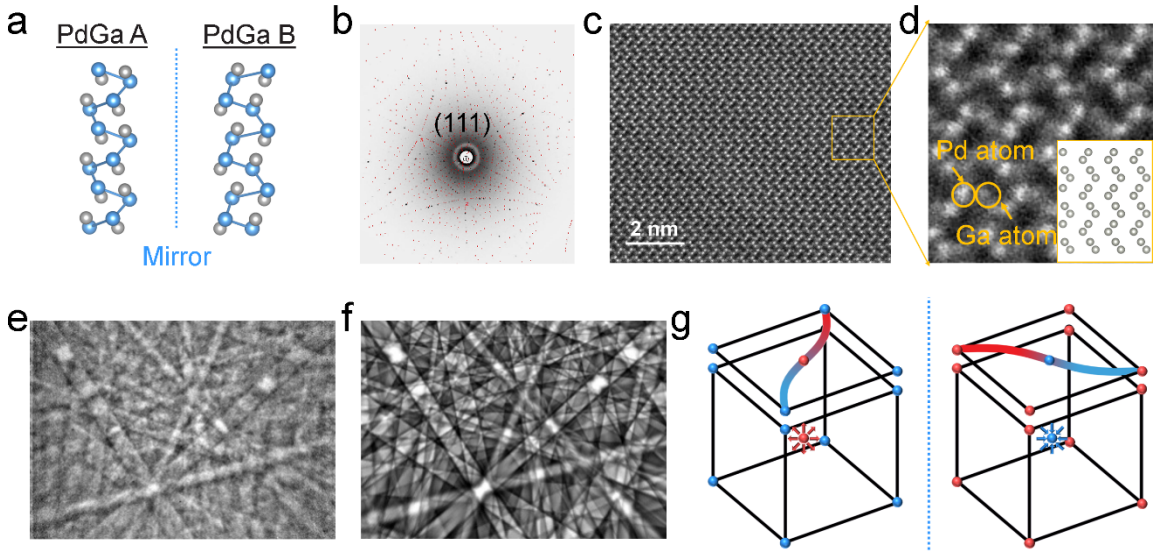

Fig. 1 a Illustration of the chiral crystal structure of both TH PdGa enantiomers. Blue and grey dots correspond to Pd and Ga atoms, respectively. **b** Laue diffraction of the TH PdGa crystal with a single (111) pattern. **c** STEM image of TH PdGa. **d** Zoomed-in image obtained from the yellow rectangle in figure c. The inset figure illustrates the arrangement of Pd atoms along the [101] direction. The white dots are Pd atoms, while the grey dots next to the Pd atoms are Ga atoms. **e** EBSD pattern and **f** simulated EBSD pattern of the TH PdGa enantiomer in A form at the EBSD01 site. **g** Schematic illustration of the chiral electronic structure of two TH PdGa enantiomers, including chiral fermions (red and blue) in the bulk BZ and of the Fermi-arcs in the surface BZ. The red and blue spheres represent Weyl fermions with opposite chiral charges.

Bulk single crystals of TH PdGa up to several centimeters in size were grown by the self-flux method. Single crystal X-ray diffraction and the Flack method were first used to analyze the crystal quality and structure. The obtained X-ray diffraction patterns along the c-axis (Supplementary Fig. 2) showed sharp and symmetrical diffraction spots, indicating excellent crystal quality, and the lattice constant was determined to be 4.8967 Å. More comprehensive details regarding the single crystal X-ray diffraction analysis can be found

in our previous work.[23, 27] Subsequently, Laue X-ray diffraction was performed for both TH PdGa enantiomers derived from different batches of as-grown crystals. Remarkably, both TH PdGa enantiomers exhibited sharp and well-defined Laue diffraction spots, corresponding to a single pattern of (111) faces. This indicated the presence of single crystallinity and homochirality without any twinning or domains (Fig. 1b and Supplementary Fig. 3). To gain a deeper insight into the atomic arrangement of TH PdGa, a thin lamella sample for scanning transmission electron microscopy (STEM) was fabricated by focused ion beam (FIB) technique. The white spots in the STEM images refer to the heavy Pd atom, while the grey spots next to Pd atoms can be assigned to the Ga atom (Fig. 1c, d). The Pd-Ga atomic stacking sequence matched well with the simulated atomic arrangement along the (101) direction, with 100% occupancy of the Pd and Ga sites (inset figure in Fig. 1d). With the perfect crystal structure of the $P2_13$ group, the handedness of the PdGa single crystals was then distinguished by electron backscatter diffraction (EBSD). Each TH PdGa crystal, PdGa A and PdGa B, showed only one chirality at various detection spots, further confirming the homochirality of the whole single crystals (Fig. 1e-f, Supplementary Fig. 4 and Supplementary Fig. 5). Furthermore, Figure 1g shows a schematic of two oppositely charged (chiral) Weyl fermions in the bulk and a reversal of the propagation direction of the Fermi-arc at the surface Brillouin zone (BZ). The multifold fermions at the Γ and R points act as sources (positive Chern number) or sinks (negative Chern number) of the Berry curvature, indicating the chiral electronic structure of TH PdGa.[23]

ORR reactivity of TH PdGa

Having established the well-defined topological homochiral structure of the TH PdGa, we then investigate its ORR catalytic activity. The electrochemical performance of TH PdGa was evaluated in 0.1 M aqueous $HClO_4$ solution. Commercial Pt/C and achiral PdGa (AC PdGa) were used as reference materials for comparison. The AC PdGa showed a polycrystalline structure without any impurities (Supplementary Fig. 6 and Supplementary Fig. 7). Linear sweep voltammetry (LSV) was first performed to evaluate the ORR activity in an O_2-saturated $HClO_4$ electrolyte with the continuous oxygen flow. As shown in Fig. 2a, the TH PdGa demonstrates the best ORR activity in terms of the onset potential (E_{onset}) and the $E_{1/2}$. Specifically, TH PdGa reaches the highest E_{onset} of 1.01 V *vs.* RHE and the

most positive $E_{1/2}$ of 0.89 V *vs.* RHE, outperforming Pt/C with 0.94 V *vs.* RHE and 0.80 V *vs.* RHE for the E_{onset} and $E_{1/2}$, as well as AC PdGa with 0.89 V *vs.* RHE and 0.79 V *vs.* RHE for the E_{onset} and the $E_{1/2}$, respectively (Fig. 2b). The limited current density of TH PdGa was enhanced by approximately 35% at a potential of 0.4 V *vs.* RHE when compared to AC PdGa. The kinetic current density (J_k) at a higher potential of 0.85 V *vs.* RHE was calculated, among which TH PdGa exhibited the highest J_k of 137.02 mA cm^{-2}. This J_k value was remarkably superior to Pt/C (1.97 mA cm^{-2}) and AC PdGa (0.49 mA cm^{-2}) by almost 70- and 280-fold, respectively. The Tafel slope serves as a valuable parameter for assessing the kinetics of the ORR. Notably, the TH PdGa electrode exhibits the smallest Tafel slope (84.8 mV dec^{-1}) compared to both Pt/C (210.3 mV dec^{-1}) and AC PdGa (112.2 mV dec^{-1}) (Supplementary Fig.9). This observation further suggests that the TH PdGa electrode has the fastest ORR kinetics. A comprehensive comparison is presented in Fig. 2c, showing the state-of-the-art ORR activity in acidic conditions in terms of $E_{1/2}$ and J_k. Remarkably, the TH PdGa exhibits superior catalytic activity in comparison to previously reported nanostructured ORR catalysts with substantial surface areas. These results highlight the pivotal role of the chiral induced spin polarization effect in bulk inorganic crystals for enhancing the ORR kinetics and overall activity. For a deeper understanding of the intrinsic reactivity of the samples, the experimental ORR activities were further analyzed through deconvolution into the intrinsic turnover frequency (TOF). Notably, the TH PdGa demonstrated an impressive TOF of 16.1 s^{-1}, which exceeds the TOF of Pt/C and AC PdGa by more than 200 times (Fig. 2d). These results reinforce the notion that the remarkable enhancement in ORR activity is attributed to the spin-polarized electrons in the TH PdGa, rather than other contributions, given its well-defined single crystal structure with robust TSS against extrinsic modifications.

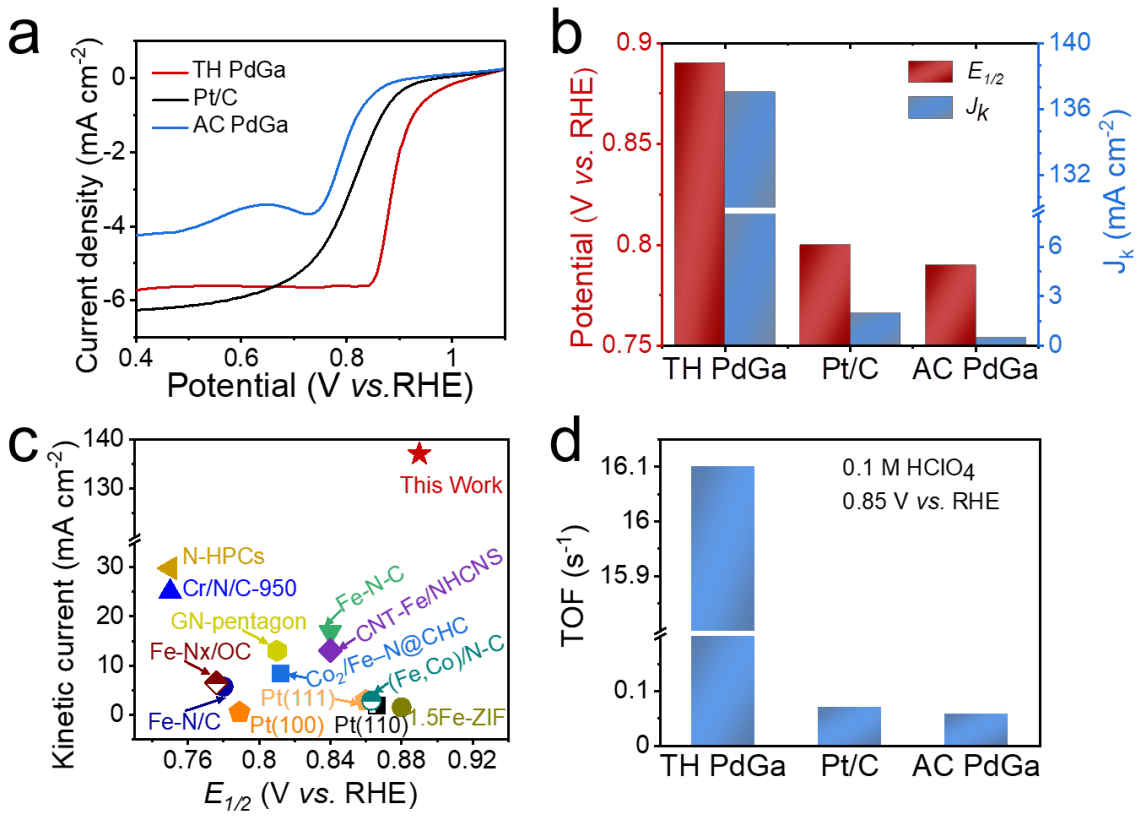

Fig. 2 a LSV polarization curves of TH PdGa, Pt/C and AC PdGa samples. **b** $E_{1/2}$ and J_k at 0.85 V *vs.* RHE for TH PdGa, Pt/C and AC PdGa. **c** Comparison of the $E_{1/2}$ and J_k of TH PdGa and reported state-of-the-art ORR catalysts in acidic media. **d** Comparison of TOF values of TH PdGa, Pt/C and AC PdGa for ORR at 0.85 V *vs.* RHE.

ORR selectivity on TH PdGa

The selectivity of the ORR can be effectively evaluated by monitoring the production of H_2O_2, a key indicator that is expected to be reduced on chiral catalyst surfaces due to the CISS effect.[10, 11] To measure the H_2O_2 yield, UV-visible spectrophotometry was employed after a 1-hour chronoamperometric test (Fig. 3a). The results showed a significant reduction in the H_2O_2 yield in the presence of the TH PdGa sample, as depicted in Fig. 3b. This decrease can be attributed to the fact that the formation of H_2O_2 (a singlet species) is spin-forbidden on a spin-polarized chiral surface. This phenomenon is consistent with the previously reported CISS effect observed in water splitting.[12, 15, 28, 29] During the ORR process, the OH intermediates formed from O_2 will exhibit different spin states depending on the chirality of the catalyst surface. In particular, on an achiral catalyst surface, the

unpaired electrons of OH intermediates display mixed spin states. As a result, the OH intermediates in their doublet ground state can interact with each other, allowing for the formation of H_2O_2. On a homochiral catalyst surface, however, the unpaired electrons of the OH intermediates are aligned in a parallel fashion so that the formation of H_2O_2 is symmetry forbidden (Fig. 3c). This intriguing behavior highlights the role of the chiral-induced spin polarization in governing the selectivity of the ORR and sheds light on the unique catalytic properties of the TH PdGa sample.

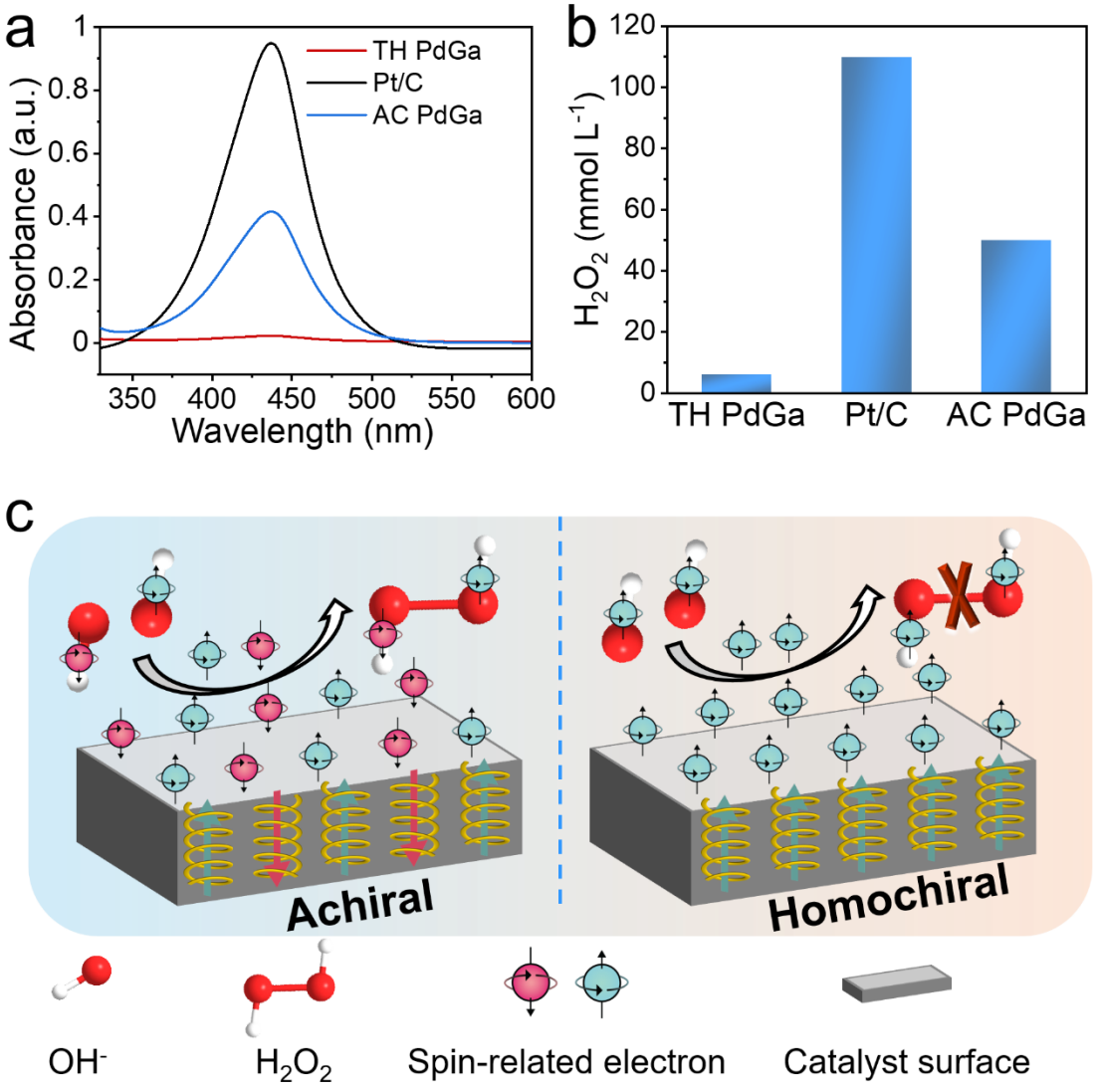

Fig. 3 a UV-visible spectrophotometric analysis of H_2O_2 production from chronoamperometry at 0.5 V *vs.* RHE on TH PdGa, Pt/C and AC PdGa. **b** Comparison of

H_2O_2 concentration in the electrolyte for TH PdGa, Pt/C and AC PdGa, respectively. **c** Illustration of the spin polarization induced by the homochiral crystal structure for the enhanced ORR selectivity. When the electrons transferred from the achiral catalyst surface have both spin states, the spins of the unpaired electrons on the two OH• are aligned antiparallel, so the interaction between the two OH• is on a singlet surface and it is easy to produce H_2O_2. When the electron transferred from the catalyst surface is spin dependent, the spins of the two electrons are aligned parallel to each other, so the two OH• interact on a triplet surface, inhibiting the formation of H_2O_2 and facilitating the 4^- electron process.

Spin polarization in TH PdGa

The spin polarizations in the TH PdGa crystals were directly probed in spin-resolved photoemission measurements. Photoelectrons were excited with deep-UV laser pulses at λ = 213 nm ($h\nu$ = 5.83 eV) and their average spin polarization was measured in a Mott scattering apparatus (Methods).[30, 31, 32] Fig. 4 a, b show representative spin polarization distributions measured on the (001) surfaces of two TH PdGa enantiomers with opposite chirality. Each count in the histograms represents approximately 10^4 detected electrons. For TH PdGa A and TH PdGa B, the average spin polarizations were determined to be P = (−2.0±4.1) % and P = (+2.7±4.3) %, respectively when excited with s-linearly polarized light. The charge carrier density in TH PdGa shows an order of 10^{20} cm^{-3}, the spin polarization concentration in TH PdGa is of the order of 10^7 times that of the artificial chiral catalytic surfaces.

In materials with strong SOC, spin-polarized photoelectrons can also be excited by circularly polarized light. These non-zero spin polarizations arise from the selection rules that determine specific final spin states within a non-degenerate band structure. It is important to note that the spin polarization values shown in Fig. 4a, b were measured using linearly polarized light, with light incidence and electron emission along the surface. The measured spin polarization values therefore directly reflect the intrinsic, chirality-induced symmetry breaking of the TH PdGa surfaces. This interpretation is further supported by the observed correlation between the sign of the spin polarization and the specific PdGa enantiomer, as expected from symmetry considerations.[18]

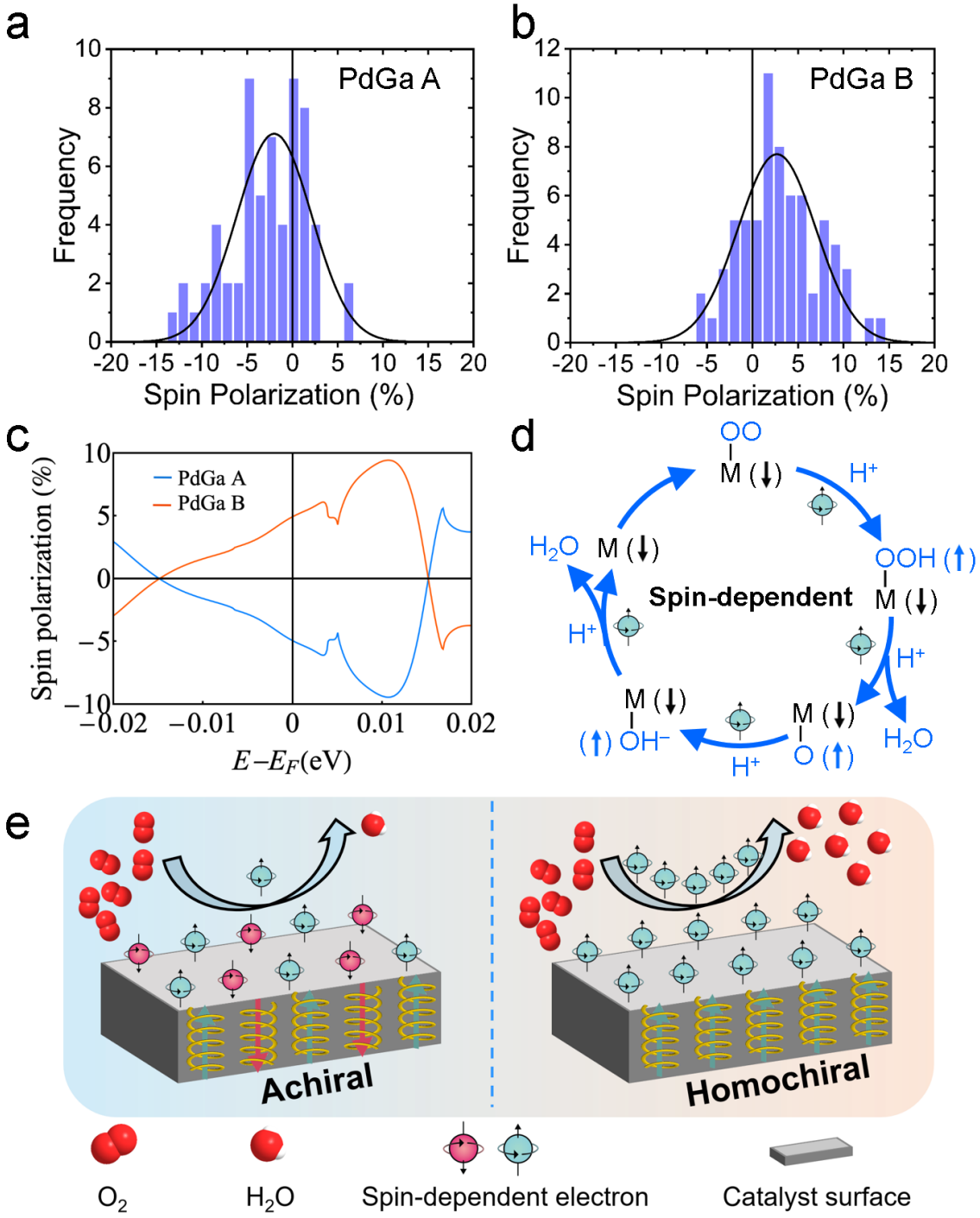

Fig. 4. Photoelectron spin polarization distributions measured on **a** TH PdGa A and **b** TH PdGa B surfaces. Photoelectrons were excited with linearly polarized light. Average spin polarization values are determined from Gaussian functions fitted to the distributions. **c** Spin polarization calculated with Eq. (1) with an inset around the Fermi level, where the polarization is −4.92% for TH PdGa A and +4.92% for TH PdGa B respectively. **d** Spin-

dependent electron transfer process in the ORR on a chiral PdGa surface. **e** Illustration of the CISS effect on the enhanced ORR activity.

In addition to the non-zero photoelectron spin polarization, chiral materials can exhibit a circular dichroism in the photoelectron yield. To check for such an asymmetry, the light polarization was interchanged between s-linear, clockwise (cw) and counterclockwise (ccw) circular throughout the measurement procedure. For each polarization, the count rates of both detectors inside the Mott polarimeter were summed up, yielding $I_{\mathrm{cw,ccw}}^{\mathrm{total}} = (I_u + I_l)_{\mathrm{cw,ccw}}$, and integrated over the entire measurement time. The dichroism was then calculated as $\Delta I = (I_{\mathrm{cw}}^{\mathrm{total}} - I_{\mathrm{ccw}}^{\mathrm{total}})/(I_{\mathrm{cw}}^{\mathrm{total}} + I_{\mathrm{ccw}}^{\mathrm{total}})$. For TH PdGa A and TH PdGa B, circular dichroism values of $\Delta I \approx (-22.6 \pm 2.1)\,\%$ and $\Delta I \approx (+9.6 \pm 0.3)\%$, respectively, were measured. This circular dichroism asymmetry further emphasizes the pronounced chiral characteristics and intrinsic chirality-induced effects present in the TH PdGa crystals.

Furthermore, theoretical modelling using a two-terminal setup and the Landauer formalism was applied to calculate spin-dependent transmission in TH PdGa. The electronic structure of the crystal was represented by a tight-binding model, taking into account the intrinsic spin-orbit interaction. The simulations were focused on a finite central region with dimensions of 15×15×30 atomic layers along the [111] direction, considering the SOC due to the d-orbitals of Pd atoms[33, 34, 35, 36] (Supplementary Note 1).

By solving the scattering problem in the central region, we obtained the total transmission, which was further decomposed into different spin components. The spin polarization was quantified as the asymmetry between the up and down spins transmitted through this region, expressed in equation (1):

$$\mathcal{P} = \frac{T_{\uparrow\uparrow}+T_{\downarrow\uparrow}-T_{\uparrow\downarrow}-T_{\downarrow\downarrow}}{T_{\uparrow\uparrow}+T_{\uparrow\downarrow}+T_{\downarrow\uparrow}+T_{\downarrow\downarrow}} \times 100 \qquad (1)$$

In equation (1), the sub-indices with arrows represent the spin directions of the incoming and outgoing electrons transported through the central region (Supplementary Fig. 10,11). The results, as shown in Fig. 4c, revealed that the spin polarizations for TH PdGa A and TH PdGa B around the Fermi level were −4.92% and +4.92%, respectively. These findings

highlight the significant role of the high SOC of Pd, coupled with the chiral structure, in generating the observed spin asymmetry (Supplementary Fig. 10). To further assess the impact of the chiral structure, we performed an additional calculation for the crystal in [001] orientation, which revealed a pronounced contrast in spin asymmetries between the chiral (4.25% for TH PdGa) and non-chiral (0.1%) structures (Supplementary Note 1, Supplementary Fig. 11). These results further underscore the importance of the chiral structure in inducing and enhancing spin asymmetry in TH PdGa.

The mechanism of the CISS effect in the bulk chiral inorganic materials for enhanced ORR kinetics is illustrated in Fig. 4d, e. During the ORR process, oxygen molecules in their triplet ground state must split to form water in singlet state. If there is no spin control on the achiral surface and electronic potential of the interaction has a triplet character, extra energy is required to transfer the electron to the O_2 because the transition is forbidden by quantum mechanics. When there is spin alignment control of electrons on the homochiral surface, the electrons on the triplet potential surface can more easily transfer through the conduction band of PdGa to the O_2. Therefore, the ORR kinetics and efficiency are promoted.

Electronic structure of TH PdGa

Apart from the electron spin, the electronic structure plays a significant role in the catalytic performance. Fig. 5a and b present the bulk band structure of TH PdGa with and without SOC throughout the BZ. The presence of SOC and the absence of inversion symmetry lead to observable band splitting with opposite spin at the G and R high symmetry points in the bulk. In particular, a four-fold degenerate Rarita–Schwinger–Weyl spin 3/2 fermion with a topological charge of Chern number +4 is found at the G point, while two three-fold degenerate double-Weyl spin 1 fermions with Chern numbers –4 are found at the R points.[23] The substantial SOC in TH PdGa causes the G and R Weyl points to approach the Fermi level, which is predicted to benefit the catalytic reactions as a result of enriched electrons and weakened bonding strength for oxygen intermediates.[37] In addition, the majority of carriers at the Fermi surface are mainly contributed by Pd, suggesting that the Fermi-arc TSS are mostly derived from d orbitals of Pd, which are believed to increase the reservoir of catalytically active electrons in the ORR catalysis process. Furthermore, the

breaking of the inversion symmetry in TH PdGa results in a larger topologically non-trivial energy window compared to AC PdGa (Supplementary Fig.12). The chiral electronic structure of PdGa is illuminated by chiral fermions and chiral Fermi-arc TSS.

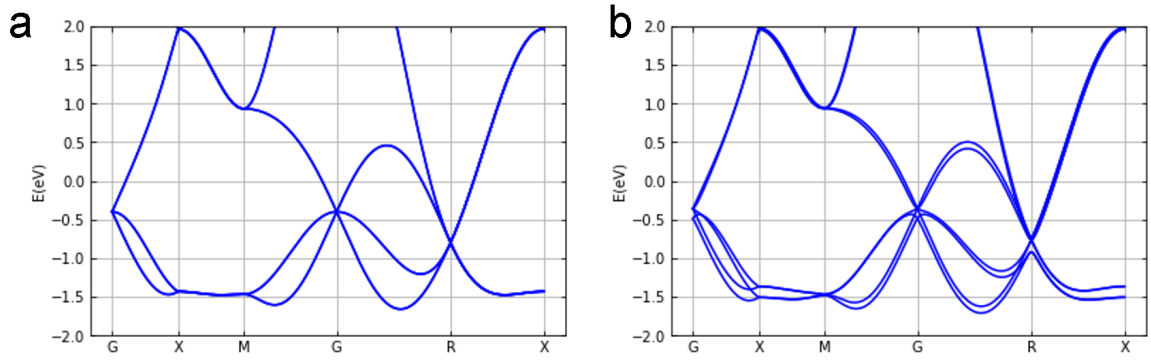

Fig.5 a Band structures of TH PdGa **a** without and **b** with inclusion of SOC effect, respectively.

The projected density of states (PDOS) of TH PdGa, as well as the PDOS of the Pd d-orbital and the Ga p-orbital, are shown in Supplementary Fig.13a. The contributions to the PDOS from the Ga d-orbital arise at energies of −15 eV, which is far from the d-orbital of Pd. However, the p-orbital of Ga overlaps with the d-band of Pd, indicating a p-d interaction rather than a d-d interaction between Ga and Pd. The extracted d-band center of the surface Pt atom in pure Pt and the surface Pd atom in PdGa are essential descriptors for ORR activity. As shown in Supplementary Fig.13b, the d-band center of PdGa (-2.369 eV) is slightly shifted downwards compared to the d-band center of pure Pt (-2.026 eV). According to the d-band theory, this downshift of the d-band center leads to a weaker bonding strength of oxygen species, thereby facilitating an improved ORR activity when compared to the strong bonding strength observed on pure Pt.[3, 38] In addition, the electron density distribution on the PdGa crystal slab shows electron accumulation around the Pd atoms, probably due to p-d charge transfer between Ga and Pd (Supplementary Fig.13c, d). Taken together, the p-d orbital interaction between Ga and Pd, the favorable band structure at the Fermi level, and the optimized adsorption strength of oxygen intermediates collectively position TH PdGa as a promising candidate for remarkable ORR performance.

Electron spin on the catalyst surface has been proven to play a substantial role in influencing electron transfer to oxygen intermediates and the bonding strength with oxygen

species.[6, 13, 39] Therefore, a comprehensive analysis of the adsorption/desorption process of chemisorbed oxygen species on TH PdGa was conducted to gain an unbiased understanding of the ORR mechanism. Typically, the rate-determining step (RDS) in ORR is the transition from O_2* to OOH* because extra energy is required for the transition from triplet O_2 to closed-shell singlet states.[4] For the Density Functional Theory (DFT) calculations (Supplementary Fig.14-15 and Supplementary Table 1), the O* (chemisorbed oxygen) coverage on the TH PdGa surface is assumed to be 1, whereas it is ½ for the AC PdGa surface due to the facilitated splitting of the triplet O_2.[38] As a result, the energy barrier of the RDS was found to be 0.838 eV for TH PdGa and 0.964 eV for AC PdGa, respectively (Supplementary Fig.16), which is consistent with an activation entropy difference of 0.128 eV, considering the electron spin effect for the chiral catalytic surface.[15]

Conclusion

In conclusion, this study reports a novel topological homochiral PdGa catalysts for the ORR in acidic media, which exhibit significantly improved reaction kinetics owing to the spin polarization at the intrinsic chiral active sites. In particular, the TH PdGa catalysts display remarkable activity with record-high values of 0.89 V for $E_{1/2}$, kinetic current density of 137.02 mA cm^{-2}, and intrinsic catalytic TOF of 16.1 s^{-1}, outperforming the reactivity of Pt/C 70 times in terms of kinetic current density and more than 200 times in terms of TOF, as well as rivaling other state-of-the-art catalysts in acidic electrolytes. The spin polarization in TH PdGa crystals is directly probed by spin-resolved photoemission experiments and theoretical modelling, which reveal opposite spin polarization values for the two TH PdGa enantiomers. The concentration of spin polarization in TH-PdGa is about 10^7 orders of magnitude higher than in catalysts with "artificial chiral catalytic surfaces". Furthermore, it is confirmed that both chirality and SOC play crucial roles in the generation of spin-polarized electrons in TH PdGa. This work also provides fundamental studies of CISS effect in bulk inorganic materials. The experimental and theoretical findings highlight the potential of these new topological chiral materials as next-generation spin-dependent catalysts, offering high efficiency and advanced selectivity in catalytic applications.

Methods

PdGa single crystal growth

The TH PdGa single crystals were grown via the self-flux technique.[23] Specifically, a polycrystalline ingot was first prepared through arc melting stoichiometric amounts of Pd and Ga metals with 99.99% purity in an argon atmosphere. Secondly, the as-prepared ingot was crushed into powder, then filled in an alumina crucible and sealed in a quartz tube. Thirdly, the entire quartz ampoule was annealed at 1100 °C for 12 h, then slowly cooled to 900 °C at a rate of 1.5 °C/h, and subsequently cooled to 800 °C at a rate of 50 °C/h, held for 120 h and then cooled to 500 °C with a rate of 5 °C/h. The obtained PdGa single crystal was cut into plate-like shape with a smooth geometry surface area of about 5 mm^2 and used as the electrode for catalysis directly.

Materials characterization

A white beam backscattering Laue X-ray diffraction was first performed to check the single crystallinity of PdGa at room temperature. The single crystal X-ray diffraction data were collected on a Rigaku AFC7 four-circle diffractometer with a Saturn 724+ CCD-detector applying graphite-monochromatized Mo-Kα radiation. A summary of the crystallographic information can be found in Table S1. A FEI Tecnai G2 F30 electron microscope with an acceleration voltage of 300 kV was used to perform STEM. UV-Vis absorption spectra were tested on an Agilent Cary 5000 UV-Vis-NIR spectrophotometer with an integration sphere. Powder X-ray diffraction (PXRD) were carried out on a STOE STADI P diffractometer with Cu Kα target (λ = 1.54178 Å).

Electrochemical measurements of ORR activity and selectivity

The electrochemical measurements were carried out on a PINE electrochemical workstation using a standard three-electrode configuration. A Pt electrode and an Ag/AgCl electrode were used as the counter and reference electrode, respectively. For chiral PdGa and achiral PdGa samples measurement, a piece of bulk crystal was mounted on the commercial rotator and used as the working electrode. For Pt/C sample measurement, homogeneous catalysts ink (20% Pt/C, Fuel cell) was drop-cast on the glassy carbon rotating disk electrode (RDE, 5 mm in diameter) with a loading of 0.25 mg cm^{-2} for

electrocatalysis. In detail, the LSV curves was conducted in the O_2-saturated 0.1 M $HClO_4$ solution with a scan rate of 10 mV s^{-1}. The ORR performances were assessed by recording LSV from 1.1 V to 0.3 V at 10 mV s^{-1} in O_2-saturated electrolytes at a rotating rate of 1600 rpm, with the negative-going curves being used for activity determination. The CV curves were recorded in Ar-saturated and O_2-saturated 0.1 M $HClO_4$ electrolytes at a scan rate of 10 mV s^{-1}, respectively. Note: Both LSV and ORR curves were recorded and presented without any iR correction. The accelerated durability test was performed by potential cycling from 0.60 to 1.00 V vs. RHE at a sweep rate of 100 mV s^{-1}.

The Nernst equation was used as the conversion formula for converting potentials from the Ag/AgCl scale to the RHE scale:

$$E_{RHE} = E_{Ag/AgCl} + 0.059 \times pH + 0.197 \quad (2)$$

The kinetic current density (J_K) was obtained from LSV measurements based on the Koutecky-Levich equation:

$$\frac{1}{J} = \frac{1}{J_L} + \frac{1}{J_K} \quad (3)$$

Where the diffusion limiting current density J_L was chosen at potential 0.4 V *vs.* RHE.

Turnover frequency calculations (TOF)

The electrochemical active surface area of the chiral PdGa electrode was estimated by measuring the double-layer capacitance at various scan rates. The specific capacitance was determined by plotting the capacitive currents as a function of the scan rate. The (111) crystal plane are regarded as the active centers with an active site density (D) of 7.02×10^{14} atoms cm^{-2}. The TOF was calculated using the kinetic current activity J_K (mA cm^{-2}) at a given electrode potential (0.85 *vs.* RHE).

The total number of oxygen atom turnovers T_O was calculated from the current density according to:

$$T_O = (j\frac{mA}{cm^2})\,(\frac{1\,Cs^{-1}}{1000mA})\,(\frac{1\,mol\,e^{-1}}{96485.3C})\,(\frac{1\,mol\,O_2}{4\,mol\,e^{-1}})\,(\frac{6.023\times 10^{23}\,O_2}{1mol\,O_2}) = 1.56\times 10^{15}\,\frac{O_2/s}{cm^2}\,per\,\frac{mA}{cm^2} \quad (4)$$

$$\text{TOF [electron site}^{-1}\,s^{-1}] = \frac{T_O \times J_K}{D \times A_{ECSA}} \quad (5)$$

Photoelectron spin polarization measurements

A simplified scheme of the Mott scattering setup is provided in Supplementary Fig.16. Deep-UV laser pulses at λ = 213 nm (hν = 5.83 eV) with a pulse length of about 200 ps. The radiation is generated as the fifth harmonic of a Nd:YVO_4 laser through frequency doubling in a lithium triborate (LBO) crystal followed by two consecutive frequency mixing steps in a second LBO crystal and a β-barium borate (BBO) crystal. The laser pulses impinge onto the sample surface along the surface normal and at a repetition rate of 20 kHz. The photoelectrons are as well collected along the surface normal by electron-optical elements and guided into the Mott polarimeter. This instrument comprises a 70 nm thin gold foil set to a potential of +50 kV. The photoelectrons are hence accelerated to weakly relativistic energies before being scattered at the foil. In consequence, the atomic nuclei of the scattering target induce a magnetic field in the rest frame of the electrons, which introduces a spin-dependent term into the scattering cross section. Since this term only depends on the projection of the spin onto the direction of the magnetic field, the Mott polarimeter is only sensitive to a transversal spin polarization. An electron-optical 90° bender therefore converts an initially longitudinal spin polarization into a transversal one that can be detected. Two semiconductor detectors are placed symmetrically around the incident electron beam at angles of ±120° to register elastically backscattered electrons. If the photoelectrons are longitudinally unpolarized, the upper and lower detector register the same count rates, I_u and I_l, whereas an asymmetry in the count rates reflects a non-zero spin polarization. This asymmetry, calculated as $A = (I_u - I_l)/(I_u + I_l)$, is connected to the spin polarization $P = A/S$ via the Sherman function $S = 0.18$ which quantifies the analyzing power of the polarimeter.

Throughout the measurement procedure, the polarization of the light is interchanged between s-linear, cw circular and ccw circular by rotation of a quarter-wave plate (QWP). At each QWP position, about 10^4 electrons are collected. The measurement position is interchanged between the sample and a molybdenum reference mounted directly underneath the sample after each full rotation of the QWP. Since molybdenum emits unpolarized electrons irrespective of the light polarization, this allows to correct for any instrumental asymmetries. To further ensure the correct alignment and stability of the

polarimeter throughout the measurement, the spin polarization of photoelectrons emitted from a sputter-cleaned Au(111) crystal surface is measured before and after each measurement procedure. From this surface, cw and ccw circularly polarized light excites photoelectrons with a well-defined spin polarization of about $P = +(-)\,25$ %. Only if these values are measured both prior to and after the measurement on the sample, the results are considered valid.

The measurements are conducted under ultra-high vacuum conditions at a base pressure of less than $5 \cdot 10^{-9}$ mbar. The entire setup is placed inside of three Helmholtz coils which compensate for the earth's magnetic field. A permalloy shielding reduces the residual magnetic fields to less than ~20 μT.

The results of the spin polarization measurements are plotted as histograms in which each count in a specific spin polarization bin represents a single measurement which includes about 10^4 electrons. The histograms typically comprise 200-300 individual measurements, i.e., about 10^6 electrons in total, and were typically acquired over an integration time of two hours. Gaussian curves are fitted to these distributions, and the average spin polarization and its uncertainty are extracted as the expectation value and the FWHM.

Data availability

The data supporting the findings of this study are available from the corresponding authors upon reasonable request.

Acknowledgements

X.W., M. P. and X.L. contributed equally to this work. The authors thank Dr. Changjiang Yi, Ralf Koban, Dr. Dong Chen and Dr. W. Schnelle for useful discussions. This work was financially supported by the European Research Council (ERC Advanced Grant No.742068 `TOPMAT'). We also acknowledge funding from the DFG through SFB 1143 (project ID. 24731007). C.F. thanks the Deutsche Forschungsgemeinschaft (DFG, German Research Foundation) for 5249 (QUAST). H.Z. thanks the Deutsche Forschungsgemeinschaft (DFG, German Research Foundation) for partial financial support via the NSF-DFG program ECHEM in project Za 110/30-1.

Author contributions

X.W and C.F. conceived and designed this work. X.W. performed the experiments and wrote the manuscript. X.L. and M.P. carried out the computations. P.V.M. and H.Z. carried out, analyzed, and interpreted the measurements on the electron spin polarization. P. M. and C. S. grew and characterized the chiral crystals. X.L., U. B., X.F., S.C., H.B. and M.P. discussed the results and participated in the preparation of the paper.

Competing Interests

The authors declare no competing interests.

Additional information

Supplementary information accompanies this paper at http://

References

1. Suntivich J, Gasteiger HA, Yabuuchi N, Nakanishi H, Goodenough JB, Shao-Horn Y. Design principles for oxygen-reduction activity on perovskite oxide catalysts for fuel cells and metal–air batteries. *Nat. Chem.* **3**, 546-550 (2011).

2. Wang XX, Swihart MT, Wu G. Achievements, challenges and perspectives on cathode catalysts in proton exchange membrane fuel cells for transportation. *Nat. Catal.* **2**, 578-589 (2019).

3. Tian X*, et al.* Engineering bunched Pt-Ni alloy nanocages for efficient oxygen reduction in practical fuel cells. *Science* **366**, 850-856 (2019).

4. Wang X*, et al.* Atomically Dispersed Pentacoordinated-Zirconium Catalyst with Axial Oxygen Ligand for Oxygen Reduction Reaction. *Angew Chem. Int. Ed.* **134**, e202209746 (2022).

5. Gong K, Du F, Xia Z, Durstock M, Dai L. Nitrogen-doped carbon nanotube arrays with high electrocatalytic activity for oxygen reduction. *Science* **323**, 760-764 (2009).

6. Gracia J. Spin dependent interactions catalyse the oxygen electrochemistry. *Phys. Chem. Chem. Phys.* **19**, 20451-20456 (2017).

7. Kettner M*, et al.* Chirality-dependent electron spin filtering by molecular monolayers of helicenes. *J. Phys. Chem. Lett.* **9**, 2025-2030 (2018).

8. Naaman R, Paltiel Y, Waldeck DH. Chiral molecules and the electron spin. *Nat. Rev. Chem.* **3**, 250-260 (2019).

9. Li J*, et al.* Spin effect on oxygen electrocatalysis. *Adv. Energy Sustainability Res.* **2**, 2100034 (2021).

10. Ghosh K*, et al.* Controlling chemical selectivity in electrocatalysis with chiral CuO-coated electrodes. *J. Phys. Chem. C* **123**, 3024-3031 (2019).

11. Mtangi W*, et al.* Control of electrons' spin eliminates hydrogen peroxide formation during water splitting. *J. Am. Chem. Soc.* **139**, 2794-2798 (2017).

12. Liang Y*, et al.* Enhancement of electrocatalytic oxygen evolution by chiral molecular functionalization of hybrid 2D electrodes. *Nat. Commun.* **13**, 3356 (2022).

13. Garcés-Pineda FA, Blasco-Ahicart M, Nieto-Castro D, López N, Galán-Mascarós JR. Direct magnetic enhancement of electrocatalytic water oxidation in alkaline media. *Nat. Energy* **4**, 519-525 (2019).

14. Jiao Y, Zheng Y, Jaroniec M, Qiao SZ. Design of electrocatalysts for oxygen-and hydrogen-involving energy conversion reactions. *Chem. Soc. Rev.* **44**, 2060-2086 (2015).

15. Sang Y, *et al.* Chirality enhances oxygen reduction. *Proc. Natl. Acad. Sci. U.S.A.* **119**, e2202650119 (2022).

16. Vadakkayil A, Clever C, Kunzler KN, Tan S, Bloom BP, Waldeck DH. Chiral electrocatalysts eclipse water splitting metrics through spin control. *Nat. Commun.* **14**, 1067 (2023).

17. Liu Y, Xiao J, Koo J, Yan B. Chirality-driven topological electronic structure of DNA-like materials. *Nat. Mater.* **20**, 638-644 (2021).

18. Yang Q, Xiao J, Robredo I, Vergniory MG, Yan B, Felser C. Monopole-like orbital-momentum locking and the induced orbital transport in topological chiral semimetals. *arXiv preprint arXiv:2307.02668*, (2023).

19. Li G, *et al.* Observation of asymmetric oxidation catalysis with B20 chiral crystals. *Angew. Chem. Int. Ed.* **62**, e202303296 (2023).

20. Hasan MZ, Chang G, Belopolski I, Bian G, Xu S-Y, Yin J-X. Weyl, Dirac and high-fold chiral fermions in topological quantum matter. *Nat. Rev. Mater.* **6**, 784-803 (2021).

21. Xu Y, *et al.* High-throughput calculations of magnetic topological materials. *Nature* **586**, 702-707 (2020).

22. Narang P, Garcia CA, Felser C. The topology of electronic band structures. *Nat. Mater.* **20**, 293-300 (2021).

23. Schröter NB, *et al.* Observation and control of maximal Chern numbers in a chiral topological semimetal. *Science* **369**, 179-183 (2020).

24. Li G, *et al.* Dirac nodal arc semimetal PtSn4: an ideal platform for understanding surface properties and catalysis for hydrogen evolution. *Angew Chem. Int. Ed.* **131**, 13241-13246 (2019).

25. Luo H, Yu P, Li G, Yan K. Topological quantum materials for energy conversion and storage. *Nat. Rev. Phys.* **4**, 611-624 (2022).

26. Sanchez DS, *et al.* Topological chiral crystals with helicoid-arc quantum states. *Nature* **567**, 500-505 (2019).

27. Sessi P, *et al.* Handedness-dependent quasiparticle interference in the two enantiomers of the topological chiral semimetal PdGa. *Nat. Commun.* **11**, 3507 (2020).

28. Zhang W, Banerjee-Ghosh K, Tassinari F, Naaman R. Enhanced electrochemical water splitting with chiral molecule-coated Fe3O4 nanoparticles. *ACS Energy Lett.* **3**, 2308-2313 (2018).

29. Im H, *et al.* Elucidating the chirality transfer mechanisms during enantioselective synthesis for the spin-controlled oxygen evolution reaction. *Energy Environ. Sci.* , (2023).

30. Göhler B*, et al.* Spin selectivity in electron transmission through self-assembled monolayers of double-stranded DNA. *Science* **331**, 894-897 (2011).

31. Möllers PV*, et al.* Spin-Polarized Photoemission from Chiral CuO Catalyst Thin Films. *ACS Nano* **16**, 12145-12155 (2022).

32. Möllers PV, Göhler B, Zacharias H. Chirality Induced Spin Selectivity–the Photoelectron View. *Isr. J. Chem.*, e202200062 (2022).

33. Sun Y, Xu Q, Zhang Y, Le C, Felser C. Optical method to detect the relationship between chirality of reciprocal space chiral multifold fermions and real space chiral crystals. *Phys. Rev. B* **102**, 104111 (2020).

34. Chang G*, et al.* Unconventional chiral fermions and large topological Fermi arcs in RhSi. *Phys. Rev. Lett.* **119**, 206401 (2017).

35. Robredo I*, et al.* Cubic Hall viscosity in three-dimensional topological semimetals. *Phys. Rev. Res.* **3**, L032068 (2021).

36. Groth CW, Wimmer M, Akhmerov AR, Waintal X. Kwant: a software package for quantum transport. *New J. Phys.* **16**, 063065 (2014).

37. Yang Q, Li G, Manna K, Fan F, Felser C, Sun Y. Topological engineering of Pt-group-metal-based chiral crystals toward high-efficiency hydrogen evolution catalysts. *Adv. Mater.* **32**, 1908518 (2020).

38. Nørskov JK*, et al.* Origin of the overpotential for oxygen reduction at a fuel-cell cathode. *J. Phys. Chem. B* **108**, 17886-17892 (2004).

39. Suntivich J, May KJ, Gasteiger HA, Goodenough JB, Shao-Horn Y. A perovskite oxide optimized for oxygen evolution catalysis from molecular orbital principles. *Science* **334**, 1383-1385 (2011).